NASA Technical Memorandum 88237

High Speed Viscous Flow Calculations About Complex Configurations

Denny S. Chaussee

April 1986

National Aeronautics and
Space Administration

NASA Technical Memorandum 88237

High Speed Viscous Flow Calculations About Complex Configurations

Denny S. Chaussee, Ames Research Center, Moffett Field, California

April 1986

National Aeronautics and
Space Administration

Ames Research Center
Moffett Field, California 94035

HIGH SPEED VISCOUS FLOW CALCULATIONS ABOUT COMPLEX CONFIGURATIONS

Denny S. Chaussee
NASA Ames Research Center, Moffett Field, California 94035, USA

SUMMARY

A review of past parabolized Navier-Stokes applications is presented. The equations, boundary conditions, the numerical method and the grid generation are all discussed. Results ranging from the low supersonic regime to the hypersonic regime are included.

1. INTRODUCTION

The intent of this long-term project has been to develop a CFD tool that will be capable of analyzing the viscous supersonic/hypersonic flow about realistic configurations. To meet this challenge, a technique was developed that is capable of predicting the flow in regions of canopies, wings, and canards in addition to the usual simple symmetric configurations. The technique also had to allow for interactions between aerodynamic surfaces such as the vortex interaction between canards and wings.

The NASA Ames Parabolized Navier-Stokes (PNS) code was used as the mainline procedure to simulate numerically the viscous supersonic flow over these generic configurations. The parabolized approximation to the Navier-Stokes equations assumes that the flow is supersonic in the streamwise direction, and that the subsonic flow in the viscous sublayer is always positive in the streamwise direction. Thus, flows with large streamwise separation and flow reversals are excluded from treatment under the foregoing assumptions. However, crossflow separations are permitted.

Under these assumptions, the Navier-Stokes equations become parabolic in the streamwise direction, enabling a marching solution procedure which is computationally desirable and efficient. The form that is presented here was developed by Schiff and Steger (Ref. 1). It differs from the first finite-difference implicit marching algorithm in delta form of Vigneron et al. (Ref. 2) in the way in which the streamwise convection flux vector is treated. The turbulence model that has been used in this project is the Baldwin-Lomax model (Ref. 3). In some cases the turbulence model was modified to allow for a better comparison with experiment in the supersonic range. The boundary conditions are the usual viscous no-slip at the wall and a characteristic procedure is used to fit the bow-shock wave which is the outermost boundary. Since the equations are cast in conservation-law form, all discontinuities within the flow domain are predicted accurately. Owing to the possible complex nature of the configuration at each axial location as one proceeds down the body, an elliptic grid generator is employed to discretize the flow domain. In addition, an equilibrium air capability has been incorporated into the code. It uses the curve fits of Tannehill et al. (Ref. 4). Body shapes that have been marched over by the present algorithm include pointed cones (Ref. 5), sphere-cones (Ref. 6), three-dimensional reentry vehicles (Refs. 6-8), an ogive-cylinder-boattail (Ref. 9), a delta-wing configuration (Refs. 2, 10), the X-24 lifting body (Ref. 7), the Space Shuttle (Ref. 11), finned configurations (Refs. 5, 12), and, most recently, a generic fighter configuration (Refs. 13, 14). A representative number of these results are included in the present work.

2. GOVERNING EQUATIONS

The governing equations in the two base coordinate systems (Fig. 1) are transformed under a generalized coordinate mapping

$$\begin{aligned} \xi &= \xi(a) \\ \eta &= \eta(a,b,c) \\ \zeta &= \zeta(a,b,c) \end{aligned} \tag{1}$$

where the system (a,b,c) is either the Cartesian or cylindrical coordinate. The surface $\zeta = 0$ is the body surface, and a ζ = constant surface is the outer boundary or the bow-shock surface. Since the solution is marched along the axial direction, a, the ξ = constant surface is chosen to be the axis-normal crossflow plane; therefore, ζ is not a function of b or c.

For the Cartesian form a, b, and c are more commonly known as x, y, and z. In many cases, the cylindrical form provides a better choice of governing equations than the Cartesian for the particular geometry of concern. And, for that reason, this report and the code contain both the Cartesian and cylindrical form of the Navier-Stokes equations. In the cylindrical form a, b, and c are cylindrical coordinates x, θ, and r. Where r is the length of a ray extending from the x-axis in a constant x plane, and θ is the angle of that ray with the y-axis ($z = 0$) corresponding to the constant x plane.

In the thin-layer approximation, viscous diffusion in the axial direction as well as along the surface of the body in the crossflow plane (η-direction) is neglected. The thin-layer approximation used

here as a starting point is not essential to the development of the PNS equations. Tests of high-Reynolds-number flow in two dimensions ($Re = 10^4$) have always shown that the additional terms left out because of the thin-layer approximation cannot be detected to four-place accuracy in a typical finite-difference solution. Finally, the approximation termed the "parabolized approximation" is used. The diffusion terms in the marching direction, ξ, are neglected. A relatively stable marching procedure results if the following conditions are satisfied: 1) the outer inviscid flow region is supersonic relative to the downstream marching coordinate; 2) the viscous layer does not separate in the marching direction; and 3) the sublayer model of Schiff and Steger (Ref. 1) is used.

By invoking these approximations, the normalized Reynolds averaged Navier-Stokes equations transform under the generalized mapping as follows:

$$\frac{\partial \hat{E}}{\partial \xi} + \frac{\partial \hat{F}}{\partial \eta} + \frac{\partial \hat{G}}{\partial \zeta} + \hat{S} = \frac{1}{Re}\frac{\partial \hat{G}_v}{\partial \zeta} + \hat{S}_v \tag{2}$$

The vectors $\hat{E}$, $\hat{F}$, and $\hat{G}$ represent the inviscid flux vectors in the three transformed directions. They are written as,

$$\hat{E} = \frac{1}{J}\begin{bmatrix} \rho U \\ \rho Uu + \xi_a p \\ \rho Uv + \xi_b p \\ \rho Uw + \xi_c p \\ (e + p)U \end{bmatrix}, \quad \hat{F} = \frac{1}{J}\begin{bmatrix} \rho V \\ \rho Vu + \eta_a p \\ \rho Vv + \eta_b p \\ \rho Vw + \eta_c p \\ (e + p)V \end{bmatrix}, \quad \hat{G} = \frac{1}{J}\begin{bmatrix} \rho W \\ \rho Wu + \zeta_a p \\ \rho Wv + \zeta_b p \\ \rho Ww + \zeta_c p \\ (e + p)W \end{bmatrix}, \quad \hat{q} = \frac{1}{J}\begin{bmatrix} \rho \\ \rho u \\ \rho v \\ \rho w \\ e \end{bmatrix} \tag{3}$$

where $\hat{q}$ is the vector of dependent variables. In these expressions, ρ and p represent the density and pressure, respectively. The variables v and w are the velocity components in the y and z directions for Cartesian coordinates, and in the θ and r directions for cylindrical coordinates. u is the velocity component in the x direction. The vectors $\hat{S}$ and $\hat{S}_v$ in Eq. (2) are source terms because of the cylindrical coordinate formulation. When using Cartesian coordinates, these vectors do not exist.

The Jacobian of the transformation, J, is related to the metrics by

$$J = \xi_a(\eta_b\zeta_c - \eta_c\zeta_b) + \xi_b(\eta_c\zeta_a - \eta_a\zeta_c) + \xi_c(\eta_b\zeta_a - \eta_a\zeta_b) \tag{4}$$

where the metric quantities are given by

$$\begin{aligned} \xi_a &= J(b_\eta c_\zeta - b_\zeta c_\eta), & \eta_a &= J(c_\xi b_\zeta - b_\xi c_\zeta), & \zeta_a &= J(b_\xi c_\eta - c_\xi b_\eta) \\ \xi_b &= J(c_\eta a_\zeta - a_\eta c_\zeta), & \eta_b &= J(a_\xi c_\zeta - a_\zeta c_\xi), & \zeta_b &= J(c_\xi a_\eta - a_\xi c_\eta) \\ \xi_c &= J(a_\eta b_\zeta - b_\eta a_\zeta), & \eta_c &= J(b_\xi a_\zeta - a_\xi b_\zeta), & \zeta_c &= J(a_\xi b_\eta - b_\xi a_\eta) \end{aligned} \tag{5}$$

The total energy, e, is defined as,

$$e = \rho\,\varepsilon + \frac{1}{2}(u^2 + v^2 + w^2) \tag{6}$$

where ε is the internal energy. The contravariant velocities U, V, and W are given as

$$U = \xi_a u + \xi_b v + \xi_c w \tag{7}$$

$$V = \eta_a u + \eta_b v + \eta_c w \tag{8}$$

$$W = \zeta_a u + \zeta_b v + \zeta_c w \tag{9}$$

The only remaining viscous flux vector after the parabolized assumptions are taken can be written as,

$$\hat{G}_v = \frac{\mu}{J}\begin{bmatrix} 0 \\ m_1 u_\zeta + m_2 \zeta_a \\ m_1 v_\zeta + m_2 \zeta_b \\ m_1 w_\zeta + m_2 \zeta_c \\ m_3 \end{bmatrix} \tag{10}$$

where the quantities m_1, m_2, and m_3 are given as,

$$m_1 = \zeta_a^2 + \zeta_b^2 + \zeta_c^2 \tag{11}$$

$$m_2 = \frac{1}{3}\left(u_\zeta \zeta_a + v_\zeta \zeta_b + w_\zeta \zeta_c\right) \tag{12}$$

$$m_3 = \frac{m_1}{2}\left(u^2 + v^2 + w^2\right)_\zeta + m_2 W + \frac{k}{\mu Pr} m_1 T_\zeta \tag{13}$$

for these equations μ, k, and T represent viscosity, thermal conductivity, and temperature. The second viscosity coefficient has been taken as $\lambda = -2/3\mu$. In the Cartesian coordinate formulation,

$$\begin{aligned} a &= x \\ b &= y \\ c &= z \end{aligned} \tag{14a}$$

and

$$\hat{S} = \hat{S}_v = 0 \tag{14b}$$

and in the cylindrical coordinate formulation,

$$\begin{aligned} a &= \bar{x} \\ b &= \theta \\ c &= r \end{aligned} \tag{14c}$$

with

$$\frac{\partial}{\partial b} = \frac{1}{r}\frac{\partial}{\partial \theta} \tag{14d}$$

and

$$\hat{S} = \frac{1}{J} S \tag{14e}$$

with

$$\hat{S}_v = \frac{1}{J} S_v \tag{14f}$$

where

$$\frac{\partial}{\partial n}\left(n = \bar{x}, r, \theta\right) \tag{14g}$$

is replaced with

$$\xi_n \frac{\partial}{\partial \xi} + \eta_n \frac{\partial}{\partial \eta} + \zeta_n \frac{\partial}{\partial \zeta} \tag{15}$$

Having defined the Cartesian and cylindrical coordinate formulations and the necessary relations in order to switch from one to the other, subsequent discussion will be carried out in the Cartesian coordinate formulation only.

Nondimensionalization

The nondimensional form of all the variables has been used throughout. They can be related to the dimensional form (denoted by the superscript ~) by the following definitions.

$$a = \tilde{a}/\tilde{a}_\infty \qquad Re = \frac{\tilde{a}_\infty \tilde{\rho}_\infty \tilde{L}}{\tilde{\mu}_\infty}$$

$$u = \tilde{u}/\tilde{a}_\infty \qquad Pr = \frac{\tilde{a}_\infty^2 \tilde{\mu}_\infty}{\tilde{T}_\infty \tilde{k}_\infty}$$

$$v = \tilde{v}/\tilde{a}_\infty \qquad T = \tilde{T}/\tilde{T}_\infty$$

$$w = \tilde{w}/\tilde{a}_\infty \qquad \mu = \tilde{\mu}/\tilde{\mu}_\infty \tag{16}$$

$$\rho = \tilde{\rho}/\tilde{\rho}_\infty \qquad k = \tilde{k}/\tilde{k}_\infty$$

$$e = \tilde{e}/\tilde{\rho}_\infty \tilde{a}_\infty^2 \qquad \epsilon = \tilde{\epsilon}/\tilde{a}_\infty^2$$

$$p = \tilde{p}/\tilde{\rho}_\infty \tilde{a}_\infty^2$$

The subscript ∞ refers to values of the freestream. The value of the dimensional length $\tilde{L}$ is generally taken as one unit of length (unity), and thereby allows one to work with dimensional lengths which can present less of a problem when coding the geometry, or when reading output. The nondimensional quantity, Pr, is a form of the Prandtl number and for a perfect gas is related to the Prandtl number by $Pr = (\gamma - 1)Pr$.

Closure

The system of equations is closed with an appropriate equation of state and with the definition of properties. Real gas effects must not be neglected at high Mach numbers or for high heating cases. It is in these cases that the perfect gas assumption and constant property assumptions are invalid. Therefore, an appropriate equation of state must be used. A generalized equation of state can be written in the form,

$$\tilde{p} = \tilde{p}(\tilde{\epsilon}, \tilde{\rho}) \tag{17}$$

or in a more specific form,

$$\tilde{p} = (\bar{\gamma} - 1)\tilde{\rho}\tilde{\epsilon} \tag{18}$$

where

$$\bar{\gamma} = \bar{\gamma}(\tilde{\epsilon}, \tilde{\rho}) \tag{19}$$

Here $\bar{\gamma}$ is the ratio of specific enthalpy to specific internal energy. It is only for a perfect gas that this ratio is a constant and equal to the ratio of specific heats, γ.

The expression of the pressure as a function of internal energy and density simplifies the calculation because both internal energy and density can be directly expressed in terms of the dependent variables. In contrast, an equation of state that is dependent on temperature requires more computation since temperature is not a dependent variable and, in general, is not a readily known function of the dependent variables.

The three relations needed to close the set of equations are the relation of temperature, viscosity, and thermal conductivity to the dependent variables.

$$\tilde{T} = \tilde{T}(\tilde{\epsilon}, \tilde{\rho}) \tag{20}$$

$$\tilde{\mu} = \tilde{\mu}(\tilde{\epsilon}, \tilde{\rho}) \tag{21}$$

$$\tilde{k} = \tilde{k}(\tilde{\epsilon}, \tilde{\rho}) \tag{22}$$

Again the relation to $\tilde{\epsilon}$ and $\tilde{\rho}$ simplifies the calculation.

A variable that is needed for the calculation of Mach number is the speed of sound, a. The speed of sound is a direct result of the governing equations, including the equation of state. For consistency, the speed of sound should be derived from the governing equations, and not approximated with a curve fit

or a table look-up of experimental data. An eigenvalue analysis reveals the speed of sound. For the generalized equation of state in Eq. (17), the speed of sound is found to be

$$a = \left.\frac{\partial p}{\partial \epsilon}\right|_{\rho} \frac{p}{\rho^2} + \left.\frac{\partial p}{\partial \rho}\right|_{\epsilon}^{1/2} \tag{23}$$

If the pressure derivatives in the calculation of the speed of sound are handled in the same manner as in the rest of the code, then consistency is assured. With this reasoning, the equation of state should not only return accurate values of pressure, but should also return accurate values of the first derivative of pressure. However, if the fluid is operating under the perfect gas equation of state, then the perfect gas relations

$$\tilde{a} = \sqrt{\gamma \frac{\tilde{p}}{\tilde{\rho}}}$$

$$C_p \tilde{T} = \frac{\tilde{a}^2}{\gamma - 1} \tag{24}$$

are used.

3. BOUNDARY CONDITIONS

Boundary conditions must be applied at: (1) an initial plane of data at ξ = constant, (2) both extremes of the computational domain in the ζ-coordinate, and (3) at two planes of data in the circumferential (η) direction (unless periodic).

An accurate initial data solution is needed. The parabolized Navier-Stokes prediction procedure can generate its own appropriate starting solution for conical bodies, or it can be started from a time dependent blunt-body program. Both options are discussed subsequently.

The boundary conditions specified at the surface of the body always include the no-slip and no-blowing conditions. Options are available that allow specifications of either an assigned wall temperature or an adiabatic wall condition.

For symmetric bodies at zero angle of yaw, the symmetry conditions in the $\eta = 0$ and $\eta = \eta_{max}$ planes are imposed. Otherwise, periodic boundary conditions are imposed in η. Although the periodicity condition requires more computer storage, it is the easiest boundary condition to impose implicitly in the η-direction without stability problems.

The outer boundary of the computational domain is either specified as a known free stream or as the peripheral bow shock which is determined as the solution is marched downstream. Shock-fitting logic is used in the latter case.

The various boundary conditions are discussed in the following subsections: the initial conditions, the body-boundary conditions, shock-fitting procedures, and the circumferential boundary conditions.

Initial Data

Consider a flowfield which starts at an initial plane defined by ξ_2 = constant and extends downstream to larger values of ξ. Two planes of data are required to start the calculations, one at ξ_1 = constant and the second at ξ_2 = constant (where $\xi_1 < \xi_2$). In general, each of the initial planes will be divided into a grid defined by combinations of ζ,η coordinates. Initial flowfield data given in the format ρ, ρu, ρv, ρw, and e are to be supplied at each of the ξ,ζ,η grid points. Here, the Cartesian-velocity components are employed and the variables are not normalized by Jacobians. It is not necessary that the initial data be supplied on a grid which is exactly the same as the one to be used downstream, since the PNS code will automatically interpolate the initial data onto an appropriate grid.

There are always potential problems when numerical solutions are matched along a common boundary. Inconsistencies can be generated by differences in the governing equations, the solution procedures, the computational grids, or any number of other sources. A commonly encountered systematic error is introduced when the blunt-body procedure does not include a constant pressure, viscous-sublayer model. Even when the prediction procedures are well matched, significant errors can be introduced by the interpolation from one grid to the other. With a little forethought and judgment, the careful investigator should be able to keep the effects of such inconsistencies well within the truncation error which is always present in the downstream PNS solution.

For body configurations at moderate angles of attack and yaw, and almost conical in shape near the nose, one can use the conical approximation to obtain starting data. Indeed, by employing the so-called step-back principle, one can use the PNS code to self-start the calculations. This principle is based on the supersonic cone rule at zero angle of attack, which is approximate for turbulent flow and exact for laminar flow. The essential idea is that the solution over the conical part of the body near the nose can

be approximated by the solution over an equivalent pointed cone. Therefore, the similarity principle applies, and the solution is only a function of the similarity coordinate and varies over the downstream distance by a scaling factor only. The flow, being self-similar, can therefore be calculated by an iterative technique. Using such an approach, one advances the data from ξ station j to $j+1$ and then resets the flowfield solution back to j at an η and ζ station along the same conical ray. The flow variables are continuously readvanced to $j+1$ and then set back until a steady-state solution is reached. It is understood that this is only correct in the inviscid case. The slight error in the boundary layer thickness caused by this approximation in the viscous case is willingly accepted because of the computational efficiency involved.

Axisymmetric and three-dimensional viscous, blunt-body solutions from which to start the PNS program can be obtained using the time-dependent, blunt-body code developed by NASA Ames (Refs. 15, 16). The blunt-body program requires that the computational volume completely encompass the embedded subsonic region at the nose of the vehicles. At small angles of attack, i.e., $\alpha \leq 30$ for many blunted vehicles, the entire embedded subsonic region will be on the spherically tipped portion of the nose. Such solutions can be rotated and used at other angles of attack, provided that the embedded region remains on only the spherically tipped region of the nose.

Body Boundary Condition

For a viscous calculation, five boundary conditions must be specified at the body. The no-slip condition supplies three of these since all three velocity components must be zero at the wall. Boundary-layer theory provides the fourth as the pressure derivative is zero in the normal direction to the body surface. The fifth boundary condition is the specification of either a wall temperature, or the specification of a heat flux. For the specified wall-temperature case, the boundary conditions can be written in the form

$$\begin{bmatrix} \rho_1 u_1 \\ \rho_1 v_1 \\ \rho_1 w_1 \\ (p_2 - p_1) - \alpha(p_3 - p_2) \\ T_1 - T_{wall} \end{bmatrix} = 0 \tag{25}$$

where the subscripts are associated with l and denote the grid point number in the ζ-direction. T_{wall} is the specified wall temperature. Here α is 0 or 1/3 for first- or second-order accuracy. The specified heat flux case can be expressed as a specified temperature gradient at the wall if radiation effects are neglected. The velocity, pressure and temperature-gradient boundary conditions can be expressed as

$$\begin{bmatrix} \rho_1 u_1 \\ \rho_1 v_1 \\ \rho_1 w_1 \\ (p_2 - p_1) - \alpha(p_3 - p_2) \\ (T_2 - T_1) - \alpha(T_3 - T_2) + (1 - \alpha)\dfrac{\partial T}{\partial \zeta} \end{bmatrix} = 0 \tag{26}$$

Here, $\partial T/\partial \zeta$ is the specified temperature gradient.

For the body boundary conditions to be imposed implicitly, they must be linearized in space. This is done using the same linearization techniques given in Ref. 1; then the linearization of either Eqs. (25) or (26) can be written as

$$\Gamma^{j+1} = \Gamma^{j} + \frac{\partial \Gamma}{\partial q}\Delta q \tag{27}$$

After an implicit marching step is taken the body boundary conditions are further imposed explicitly by accepting the implicit results at $l = 2$ and solving Eqs. (25) and (26) for the variables at $l = 1$.

Outer Boundary Condition

The outer boundary associated with the computational grid plane of points, where ζ is a maximum, can be handled one of two ways. The first is commonly known as shock capturing. In this method, the outer boundary is farther from the body than the bow shock and is experiencing free-stream flow. The boundary condition for this case is very straightforward, since the dependent variables are simply set to the free-stream values.

$$\hat{r} = \begin{bmatrix} \rho - \rho_\infty \\ \rho u - \rho_\infty u_\infty \\ \rho v - \rho_\infty v_\infty \\ \rho w - \rho_\infty w_\infty \\ e - e_\infty \end{bmatrix} = 0 \tag{28}$$

Again, the boundary condition is corrected explicitly after an implicit marching step is completed. As long as the outer boundary is a sufficient distance from the bow shock, this boundary condition is stable.

The second outer boundary scheme is shock fitting. In this method, the outer boundary is the bow shock. For this method, not only the fluid dynamic variables at the shock are calculated, but the variables associated with shock propagation are calculated. A new vector of dependent variables is defined as

$$\hat{q} = J^{-1}(\rho, \rho u, \rho v, \rho w, e, y_\xi, z_\xi) \tag{29}$$

where y_ξ and z_ξ are the two unknown metric quantities that define the direction of shock propagation.

For the seven unknowns at the shock, there must be seven equations. Five of the seven equations are the Rankine-Hugoniot jump conditions across the shock which can be expressed in the form

$$[\hat{G}]^{j+1} = J^{-1}(\zeta_x^{j+1}(E^{j+1} - E_\infty) + \zeta_y^{j+1}(F^{j+1} - F_\infty) + \zeta_z^{j+1}(G^{j+1} - G_\infty)) = 0 \tag{30}$$

The brackets denote a differencing across the shock, and the metric quantities are those at the point $(j + 1, k, l_{max})$.

In Eq. (30), not only are the flux vectors unknown at $j + 1$ but the metric quantities are also unknown, since they can be written in terms of the dependent variables y_ξ and z_ξ.

The fitted shock location at $j + 1$ is found in three steps. The first step is to predict a grid at $j + 1$. The shock slope at j is extrapolated to define a predicted shock location at $j + 1$. A grid system is then generated to span the gap between the body and the predicted shock. The second step is when the implicit marching step from j to $j + 1$ is complete. The shock grid points at $j + 1$ are then freed and allowed to be implicitly moved. A restriction on this movement results in the sixth equation needed at the shock.

The seventh and final equation needed to close the set of equations at the shock is the compatibility equation. This equation is derived by first multiplying Eq. (2) by the inverse of the Jacobian of the streamwise convective flux vector and then by the left eigenvector corresponding to the only positive eigenvalue in the ζ-direction at the shock. This equation represents the flow field influence on the implicit shock solution.

The compatibility equation combined with the grid point restriction and the Rankine Hugoniot equations closes the set of equations at the shock. The result is a delta form of the shock equations with a 7×7 matrix at the shock.

Before a block tridiagonal inversion can be done, the 7×7 matrix, D must be reduced to a 5×5 matrix. The shock equation can now be inverted with the interior flow-field equations to yield the implicit result of the dependent variables at $j + 1$.

An explicit correction of the shock variables is done to eliminate any linearization error that might have occurred in the implicit marching procedure. In the real gas case, this is done by accepting the implicit result of density at the shock and iterating on an appropriate set of equations to yield the remaining unknowns at the shock. The unknowns are reduced to six since density is known, and the compatibility equation must be eliminated so that there are also six. The six remaining equations are the five Rankine Hugoniot relations and the grid-point restriction equation. A Newton iteration procedure is done on these six equations until convergence of the shock dependent variables is reached.

Circumferential Boundary Conditions

Boundary conditions must be imposed at the bounding planes ($k = 1$ and $k = k_{max}$) in the circumferential direction. Two types are available--periodic and symmetric (or reflective). Periodic-boundary conditions must be employed when a nonzero-yaw angle is specified. Symmetry conditions can be employed for zero-yaw angles for configurations that are symmetric about a pitch plane. The use of a symmetry boundary will always result in much faster calculations owing to a fewer number of grid points, so this boundary condition is used whenever it is valid.

Periodic-Boundary Condition

The periodic-boundary condition assumes that, in the circumferential direction, the first plane of data is adjacent to the last, i.e., the grid is assumed to wrap around the entire body. Relations of the form

$$\delta_\eta \hat{q}|_{k=1} = \frac{1}{2}\left(\hat{q} - \hat{q}_{k_{max}}\right) \tag{31}$$

are employed to transmit this information to the solution procedure.

Symmetry Plane Boundary Condition

A second-order accurate, fully implicit set of reflective boundary conditions has been formulated and is included in the prediction procedure.

This boundary condition assumes that the flow-field is symmetric (or reflective) about the pitch plane ($y = 0$). Thus, the flow-field properties at a given (x,y,z) point are related to the flow-field properties at the corresponding reflective point $(x,-y,z)$ by

$$\begin{aligned} y &= -y \quad (\text{or } \eta = -\eta) \\ \rho(x,y,z) &= \rho(x,-y,z) \\ \rho u(x,y,z) &= \rho u(x,-y,z) \\ \rho v(x,y,z) &= -\rho v(x,-y,z) \\ \rho w(x,y,z) &= \rho w(x,-y,z) \\ e(x,y,z) &= e(x,-y,z) \end{aligned} \tag{32}$$

where the coordinate y and velocity component v change sign as they pass through the pitch plane.

Currently, all symmetry planes occur for η = constant. Boundary-condition formulations are provided for the η derivatives of the $\hat{F}$ variables, one smoothing term and the turbulence model.

4. NUMERICAL METHOD

The algorithm used in the present work is based on the Beam-Warming delta form as applied by Schiff and Steger (Ref. 1) and other researchers (Ref. 2). It is first- or second-order accurate in the marching direction and second-order accurate in the spatial directions. A fourth-order dissipation term is appended to the algorithm as is an implicit smoothing term to further enhance the stability.

The implicit matching algorithm written in delta form without implicit smoothing is

$$\begin{aligned} &[\bar{A}_s^j + (1-\alpha)\Delta\xi(\delta_\eta \bar{B}^j + \delta_\zeta \bar{C}^j - Re^{-1}\bar{\delta}_\zeta \bar{M}^j)](\hat{q}^{j+1} - \hat{q}^j) \\ &\quad = -(\bar{A}_s^j - \bar{A}_s^{j-1})\hat{q}^j + \alpha(\hat{E}_s^j - \hat{E}_s^{j-1}) - (1-\alpha)\Delta\xi \\ &\qquad \times \{\delta_\eta[\eta_x^{j+1}(E/J)^j + \eta_y^{j+1}(F/J)^j + \eta_z^{j+1}(G/J)^j] + \delta_\zeta[\zeta_x^{j+1}(E/J)^j + \zeta_y^{j+1}(F/J)^j + \zeta_z^{j+1}(G/J)^j] - Re^{-1}\bar{\delta}_\zeta S^j\} \\ &\qquad - [(\xi_x/J)^{j+1}E_p^j - (\xi_x/J)^j E_p^{j-1}] + D\hat{q}^j \end{aligned} \tag{33}$$

where δ_η and δ_ζ are central-differenced, and the fourth-order smoothing term D is defined by

$$D\hat{q}^j = \varepsilon_E \hat{A}^j (J^{-1})^j [(\nabla_\eta \Delta_\eta)^2 (J\hat{q})^j + (\nabla_\zeta \Delta_\zeta)^2 (J\hat{q})^j] \tag{34}$$

Here, ε_E, the explicit smoothing coefficient must be less than 1/16 for stability. Additionally, $\alpha = 0$ for Euler implicit and $\alpha = 1/3$ for a three-point backward difference.

An approximately factored form of Eq. (33), which retains the same order of accuracy in ξ, can be obtained if

$$[\bar{A}_s^j + (1-\alpha)\Delta\xi(\delta_\eta \bar{B}^j)](\bar{A}_s^j)^{-1}[\bar{A}_s^j + (1-\alpha)\Delta\xi(\delta_\zeta \bar{C}^j - \frac{1}{Re}\bar{\delta}_\zeta \bar{M}^j)]\Delta\hat{q}^j = \text{LHS}(33) + O(\Delta\xi)^3 \tag{35}$$

(Note: A^{-1} can degrade the factorization error if u is sufficiently small.) Upon substituting the left-hand side of Eq. (33) by the left-hand side of Eq. (35), one obtains the factored algorithm. The algorithm is solved by the sequence of implicit inversions.

$$[\bar{A}_S^j + (1-\alpha)\Delta\xi(\delta_\eta \bar{B}^j)]\Delta\hat{q}_* = \text{RHS}(33) \tag{36a}$$

$$\left[\bar{A}^j + (1-\alpha)\Delta\xi\left(\delta_\zeta \bar{C}^j - \frac{1}{Re}\,\bar{\delta}_\zeta \bar{M}^j\right)\right]\Delta\hat{q}^j = \bar{A}_S^j \Delta\hat{q}_* \tag{36b}$$

Adding implicit smoothing to Eq. (36a)

$$[\bar{A}_S^j(1 - \varepsilon_I[-J_{j+1}^{-1}(\nabla\Delta)_\eta J_{j+1}]) + (1-\alpha)\Delta\xi(\delta_\eta \bar{B}^j)]\Delta\hat{q}_* = \text{RHS}(33) + \varepsilon_I[J_{j+1}^{-1}(\nabla\Delta)_\eta J_{j+1} - J_j^{-1}(\nabla\Delta)_\eta J_j]\hat{q}_j \tag{37}$$

where if $\varepsilon_I \neq 0$, then ε is usually 2 or 3 times ε_E and then ε_E in the right-hand side of Eq. (33) is not restricted. Otherwise if $\varepsilon_I = 0$, then $\varepsilon_E \leq 1/16$ by stability theory.

5. GENERATION OF COMPUTATIONAL GRIDS

The grid-generation process must achieve several ends that include: (1) developing accurate surface representations; (2) distributing points on the body surface; and (3) generating a clustered, well-ordered, smoothly varying, interior mesh. The configurations of current interest have only moderate variations in the axial direction, which simplifies problems associated with grid generation. In general, surface-conforming grids are required to simplify application of boundary conditions and to minimize the errors inherent in the thin-layer approximation. Such errors will be kept to a minimum by having the η = constant lines coincide with the important velocity and temperature gradients occurring within the flow. It is especially important to make sure the η = constant lines do not intercept the body at highly skewed angles.

The grid-generation process is started by choosing ξ along the body axis. In fact, ξ is permitted to align with any direction roughly parallel to the body axis. For many problems, a preferred direction would be an axis parallel to the lower surface. The ξ = constant plane, in which η and ζ vary, is chosen as a plane normal to the body axis. Cartesian inertial coordinates are selected as shown in Fig. 1 such that x and ξ are coincident. This coordinate system simplifies the governing equations since ξ_y and $\xi_z = 0$. Of more importance, surface representation and grid generation are reduced to a sequence of two-dimensional problems. Continuity of the surface must be maintained from one cross section to the next, but this is usually straightforward.

The next step is to represent the surface quantitatively and distribute a surface grid along it. Accurate surface representations take advantage of the two-dimensionality of the equations. One simply represents each cross section independently, i.e., with digitized y,z-data points. Intermediate data points can be obtained by simple interpolation. Distributing grid points on the surface is also greatly simplified for the chosen coordinate system because each cross-sectional boundary curve represents a simple one-dimensional problem. Previously, it was necessary to distribute points along such curves based on prior experiences as to how the solution would develop.

Finally, a flow-field grid is generated. This can be accomplished with methods employing either algebraic equations or partial-differential equations. The algebraic methods will always require less computer-run time and are adequate for a large variety of shapes. The methods employing partial-differential equations are preferred for complex shapes to (1) make sure that the η = constant lines are (nearly) orthogonal to the surface; (2) allow clustering of grid points into isolated regions of high curvature; and (3) simultaneously satisfy constraints (implicit in the numerical method) requiring smoothness and slow variation of the Jacobians and metrics.

It should be made clear that a truly orthogonal grid at the body can be (and is) generated only when the body shape does not change with axial distance, because the flow-field grid is confined to a plane which is normal to the axis. This is a direct consequence of the two-dimensional gridding methods used throughout the prediction procedure. In this context, caution should be exercised in applying the prediction procedure to bodies having rapid variation in the axial direction.

6. RESULTS

A number of different results are presented which show the diversity of the PNS code. The flow regimes vary from a Mach number of 2 up to 25. Both laminar and turbulent flows have been considered, as well as varying angles of attack. Configurations vary from simple cone-type bodies to lifting winged bodies such as the Space shuttle or the generic supersonic cruise fighter.

The present code was used to calculate the laminar flow field around an ogive-cylinder configuration. This geometry is shown in Fig. 2. The cylinder portion begins at an axial location of $X/L = 0.677$ and has a diameter, D. The body origin is at $x = 0$. The following are the freestream conditions: $M_\infty = 25$, $Re = 17{,}000/\text{in.}$, $\alpha = 0$, the density is $0.00142\ \text{kg/m}^3$, and the temperature is 268 K. The flow conditions are well within the hypersonic range of Mach numbers and an accurate account of real gas effects is necessary.

The grid used has 120 points in the radial direction, 19 points in the meridional direction, and 518 planes in the axial direction. The marching step size was exponentially stretched from the initial value of 8.33×10^{-6} to 3.33×10^{-3}, and then held constant after an axial location of $X/L = 0.1667$.

In Fig. 2 the shock position is shown along with the body. The ratio of the shock layer thickness to the body radius is only 16% near the nose and increases downstream. This is caused by the expansion over the convex curvature of the ogive geometry. At $X/L = 0.1667$, this ratio is 35% and on the cylinder portion of the body at $X/L = 0.95$, this ratio is 115%.

The second case to be considered is the laminar hypersonic flow over a 30% blunt cone with a 5.6° cone half-angle. The free stream Mach number is 14.2; the Reynolds number is 0.62×10^6/ft; the ratio of wall temperature to the stagnation temperature is 0.29; and the angle of attack is 18°.

Figure 3 shows a comparison of the local separation line as obtained from the experiments (Ref. 17) and calculations. The experimental separation line location was determined using the oil-flow technique. Two attachment lines (defined as the lines from which the skin-friction lines diverge) coincide with the leeward and the windward meridians. In the experiment there was no evidence of any singular points at which the axial shear stress is zero. It should be noted that the matrix A is singular for zero axial velocity, and the calculations would diverge if there were a reversal in axial velocity. It was found that the total shear stress reaches a local minimum along the separation line. Figure 3 also shows that the shear stress lines are directed toward the lee in the initial portion of the flow. The region of separation starts when the lateral component of the skin friction changes sign in the lee region. Both the calculation and the experiment show that the envelope of the skin friction lines exhibits considerable curvature followed by a gradual reduction until the lines finally follow a conical generator when the flow becomes nearly conical farther downstream. Also, the skin friction lines, which converge around the separation line, emanate from the same region, and the lines near the leeside traveled through the open portion of the separated region.

A systematic study was undertaken to verify the capability of the present computer code in calculating the flow field surrounding the flaps on the aft end of the MRVs.

The configuration studied is a 14°/7° biconic vehicle as shown in Fig. 4, with nose blunting ($R_N = 0.5$) and slices on the windward and leeward sides. The control surface protrudes from the cut on the aft end of the windward side. Results are presented for $M_\infty = 10$, $\alpha = 10°$, $T_{wall} = 560°R$, and turbulent flow with $Re = 304{,}800/m$. The control surface has a maximum deflection of 15°.

A typical computational mesh consisting of 45 meridional points by 30 radially stretched points is shown in Fig. 5. As can be expected from using straight line rays, a less-than-satisfactory grid structure in the region of the flap-flat intersection exists. Using an elliptic grid generator would alleviate this problem. Also, in these figures the outermost circumferential line is the fitted bow shock, which is tracked by the PNS code.

A necessary comparison, the pitot-pressure variation through the shock layer at a specified x-station on the vehicle, is presented for experimental, inviscid, and laminar flow results. Figure 6 presents results on the lee side which is just after the biconic juncture. Good agreement between the calculated laminar results and the experimental data are apparent. Once outside the viscous layer, the inviscid results also agree quite well. It is seen that the location of the bow shock (as indicated by the abrupt drop in the pitot pressure) is predicted quite accurately by both the inviscid and viscous computations. These results show the capability of the present PNS code to predict correctly not only the surface variables, but also the flow variables inside the viscous and inviscid portions of the shock layer.

The windward (axial) centerline surface-pressure distributions from just upstream of the flap are presented in Fig. 7 for various flap angles. The flap angles are measured from the horizontal and range from -7°, which corresponds to the cut (no-flap deflection) to a maximum deflection of 15°, which corresponds to the maximum angle for no-axial flow separation attainable with the PNS code for the above turbulent-flow conditions. Note the rapid compression at the corner of the flap which signifies the location of the flap shock, followed by a lesser compression as the flow continues up the flap. These results are quantitatively correct when compared to the nonseparated experimental results of Settles et al. (Ref. 18) and also are consistent with the results presented in Ref. 19 which were for a slightly different Mach number and configuration.

Figure 8 presents a comparison between the experimental and calculated heat-transfer rates on the $\phi = 90°$ and the $\phi = 180°$ (lee side) meridians. The slight discrepancies are most likely because of a problem with predicting flow transition between laminar and turbulent flow.

The PNS code has been used to determine the viscous supersonic flow over complex configurations. One such configuration geometry consisted of a thick-finned projectile (Fig. 9). The free-stream conditions were $M_\infty = 4$, a turbulent boundary layer with $Re/L = 10^5$/in., $T_\infty = 100°R$, $T_{wall} = 540°R$, and $\alpha = 0°$ and 2°. Forty-five grid points were stretched in the radial direction, and 117 grid points were distributed in the circumferential direction. The starting solution at $x = 2.0$ in. was generated with the PNS code using the conical step-back procedure described earlier. The conical starting solution was then

marched over the cone-cylinder portion of the projectile to $x = 13.55$ in. (which is just in front of the fins).

The grids used to calculate the flow over the finned portion of the projectile were generated using an elliptic grid generator similar to the one developed in Ref. 20. This procedure furnishes both spacing and angular control of the grid lines as they approach the boundaries of the domain such as the body and the shock. Figures 10a and 10b show representative grids at various streamwise x locations. The η = constant grid lines intersect the body orthogonally. This is important for the accurate implementation of the viscous surface boundary conditions. The solution at $x = 13.55$ in. was then marched to the end of the projectile, using the type of grids shown in Figs. 10a and 10b.

Figure 11 shows the density contours obtained for a six fin case. The protrusion of the fins into the supersonic flow field causes fin shocks, shown by the clustered contours above the fins. The clustered contour levels close to the body surface, however, are caused by the large heat-transfer rates that occur because of the constant wall-temperature boundary condition that has been imposed.

In Table 1, a comparison between numerical and experimental force coefficients (Sturek, W. B., private communication, 1982) is presented for the six-finned projectile.

The numerical and experimental values of $C_{N\alpha}$ and $x_c \cdot p$ differ by less than 4%. In comparing the values of C_A, it should be kept in mind that the base drag has not been added to the numerically obtained value of C_A. It should also be noted that there are differences between the projectile geometry used in the PNS calculation and in the experiment. The experimental projectile has a blunt nose and grooves on the cylindrical portion of the forebody in order that it could fit into a sabot.

Another complex configuration is the Space Shuttle orbiter. Numerical results have been obtained for the following wind-tunnel conditions: $M_\infty = 7.9$, $\alpha = 25°$, $T_{wall} = 540°R$, $Re = 60{,}728$/in. turbulent flow. For this calculation, the Shuttle surface coordinates were obtained from Rockwell-International Corporation. The current geometry consists of the complete Shuttle: the canopy, OMS pods, and the vertical stabilizer are included.

The three-dimensional blunt-body code originally developed by Kutler et al. (Ref. 15) was used to obtain the blunt-nose solution which creates the necessary starting planes for the PNS code at $X/L = 0.0522$. This solution was then marched downstream using the elliptic grid generator to construct the grid between the body and the fitted outermost shock wave. The grid consisted of either 61 or 121 points in the meridional direction, and 45 geometrically stretched radial points. An example of the grid at an $X/L = 0.66$ is shown in Fig. 12. The outermost grid line is the bow wave, which is fitted using an implicit technique.

The computer-generated particle paths of Fig. 13 exhibit the main features of the flow field which surrounds the Shuttle. Two distinct phenomena are the vortices on the leeside of the body and the vortice owing to the strake wing.

Finally, a generic supercruise fighter configuration is considered. Numerical results for supersonic cruise at $M_\infty = 2.169$ are presented. The wind-tunnel conditions considered are such that the Reynolds number is turbulent. Adiabatic wall conditions are assumed at the body's surface. Angle of attack of 4° is considered. The absence of yaw results in a pitch plane of symmetry which reduces the computational space and, hence, the amount of central-processing-unit (CPU) time and storage requirements. The current geometry, consisting of a canopy, body, nacelle and wing, is in a form that is readily usable by the PNS code. The point distribution on each cross section was determined independently and was then used to produce a geometry file which was read into the PNS code. Intermediate cross sections were determined by simple interpolation in the axial direction. All of the figures are scaled by either the model length (L) (Fig. 14), or the local span width (b). The locations of some of the referenced cross sections are shown in Fig. 14.

A typical grid, obtained by using the elliptic mesh generator, is presented in Fig. 15. The outermost boundary is the location of the fitted bow shock. This particular grid has 61 meridional points and 45 radial points.

Figures 16 and 17 show mesh studies for two different X/L stations. Each study used 45 radial points, but varied the number of meridional points: 61, 91, and 121 for $\alpha = 4°$. The results compared well with experimental results. The coarse details of the flow field were reasonably resolved by all systems; however, for the $X/L = 0.8$ station it appears that the 121×45 grid system produces the more accurate overall results.

Recently, a numerical result for $M_\infty = 2.2$ flow past a wing-fuselage-nacelle has been completed. In Fig. 18, Cp distributions for some representative cross sections are presented. The solid line corresponds to a wing-fuselage result, the open symbols correspond to a wing-fuselage-nacelle result, and a solid symbol corresponds to experimental results. Additionally, each open symbol is the surface location of the grid points used in the calculation. As expected, the upper surface Cp distribution is not affected by the nacelle on the under surface of the wing. The Cp distribution in the vicinity of the nacelle is qualitatively correct and, for the sparse experimental data, shows a good comparison.

7. CONCLUDING REMARKS

A PNS code has been presented which was used to solve the high-speed flow about a wide variety of complex configurations. The code which has evolved over the last eight years is a viable tool to investigate the aerodynamics and the fluid physics of supersonic flow past complex configurations. Most recently, an additional capability of the PNS code has been developed. This consists of using nonbody axis normal planes to march downstream over complex configurations. At the trailing edges of lifting surfaces, this procedure might be the best since one could orient the marching planes as to march off the surfaces parallel to the trailing edges.

8. REFERENCES

1. Schiff, L. B., and Steger, J. L., "Numerical Simulation of Steady Supersonic Viscous Flows," NASA Technical Paper 1749, May 1981.

2. Vigneron, Y. C., Rakich, J. V., and Tannehill, J. C., "Calculation of Supersonic Viscous Flow over Delta Wings with Sharp Subsonic Leading Edges," NASA TM-78500, June 1978.

3. Baldwin, B. S., and Lomax, H. L., "Thin Layer Approximation and Algebraic Model for Separated Turbulent Flows," AIAA Paper 78-257, Jan. 1978.

4. Tannehill, J. C., and Mugge, P. H., "Improved Curve Fits for the Thermodynamic Properties of Equilibrium Air for Numerical Computation Using Time-Dependent or Shock Capturing Methods," NASA CR-2470, Oct. 1974.

5. Rai, M. M., and Chaussee, D. S., "New Implicit Boundary Procedures: Theory and Application," AIAA Paper 83-0123, Jan. 1983.

6. Rizk, Y. M., Chaussee, D. S., and McRae, D. S., "Computation of Hypersonic Flow around Three-Dimensional Bodies at High Angles of Attack," AIAA Paper 81-1261, June 1981.

7. Chaussee, D. S., Patterson, J. L., Kutler, P., Pulliam, T. H., and Steger, J. L., "A Numerical Simulation of Hypersonic Flows over Arbitrary Geometries at High Angle of Attack," AIAA Paper 81-0050, Jan. 1981.

8. Chaussee, D. S., and Rizk, Y. M., "Computation of Viscous Hypersonic Flow over Control Surfaces," AIAA Paper 82-0291, Jan. 1982.

9. Schiff, L. B., and Sturek, W. B., "Numerical Simulation of Steady Supersonic Flow over an Ogive-Cylinder-Boattail Body," AIAA Paper 80-0066, Jan. 1980.

10. Tannehill, J. C., Venkaptapathy, E., and Rakich, J. V., "Numerical Solution of Supersonic Viscous Flow over Blunt Delta Wings," AIAA Paper 81-0049, Jan. 1981.

11. Chaussee, D. S., Rizk, Y. M., and Buning, P. G., "Viscous Computations of a Space Shuttle Flowfield, Lecture Notes in Physics," Ninth International Conference on Numerical Methods in Fluid Dynamics, 218, 1984, pp. 148-153.

12. Rai, M. M., Chaussee, D. S., and Rizk, Y. M., "Calculation of Viscous Supersonic Flows over Finned Bodies," AIAA Paper 83-1667, July 1983.

13. Chaussee, D. S., Blom, G., and Wai, J. C., "Numerical Simulation of Viscous Supersonic Flow Over a Generic Fighter Configuration," NASA TM-86823, Dec. 1985.

14. Wai, J. C., Blom, G., and Yoshihara, H., "Calculations for a Generic Fighter at Supersonic High-Lift Conditions," AGARD Fluid Dynamics Panel Symposium on Applications of Computational Fluid dynamics in Aeronautics, France, Apr. 1986.

15. Kutler, P., Pedelty, J. A., and Pulliam, T. H., "Supersonic Flow Over Three-Dimensional Ablated Nosetips Using an Implicit Numerical Procedure," AIAA Paper 80-0063, Jan. 1980.

16. Rizk, Y. M., Chaussee, D. S., and McRae, D. S., "Numerical Simulation of Viscous-Inviscid Interactions on Indented Nose Tips," AIAA Paper 82-0290, Jan. 1982.

17. Stetson, K. F., "Experimental Results of the Laminar Boundary Layer Separation on a Slender Cone at Angle of Attack at $M_\infty = 14.2$," Aerospace Research Laboratories, Wright-Patterson AFB, Ohio, ARL 71-0127, Aug. 1971.

18. Settles, G. S., Fitzpatrick, T. J., and Bogdonoff, S. M., "A Detailed Study of Attached and Separated Compression Corner Flowfields in High Reynolds Number Supersonic Flow," AIAA Paper 78-1167, June 1978.

19. Solomon, J. M., Ciment, M., Ferguson, R. E., and Bell, J. B., "Three-Dimensional Supersonic Inviscid Flowfield Calculations on Re-entry Vehicles with Control Surfaces," AIAA Paper 77-0084, Jan. 1977.

20. Steger, J. L., and Sorenson, R. L., "Automatic Mesh-Point Clustering Near a Boundary in Grid Generation With Elliptic Partial Differential Equations," J. Computational Physics, vol. 33, Dec. 1979, pp. 405-410.

Table 1
Comparison of experimental and numerical force coefficients.

Force coefficient	Lift curve slope, C_{N_α} (per radian)	Location of center of pressure, $x_{C.P.}$ (calibers)	Axial force coefficient, C_A
Numerical	10.395	9.361	0.304
Experimental	10.750	9.745	0.297

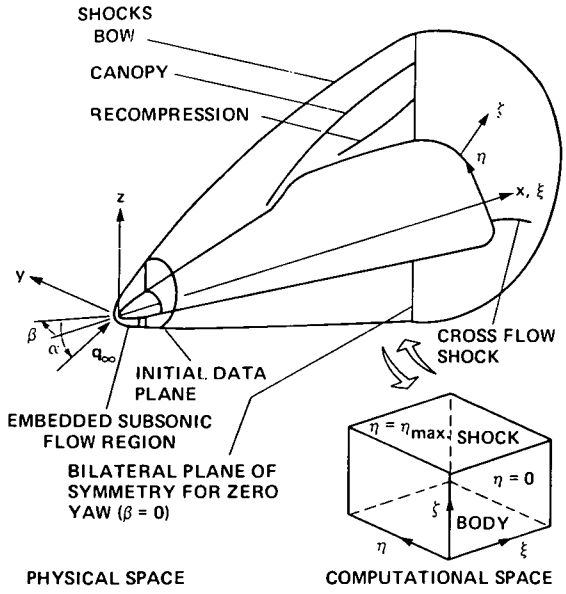

Fig. 1. Coordinate system and transformation of physical space into computational space.

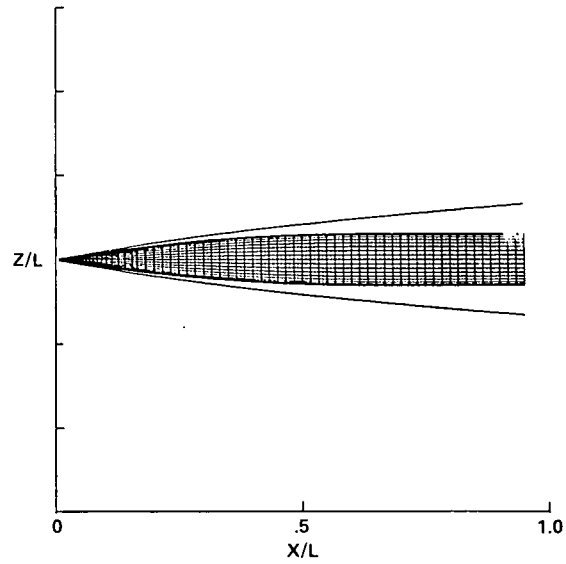

Fig. 2. Ogive-cylinder geometry and the resulting shock at Mach 25.

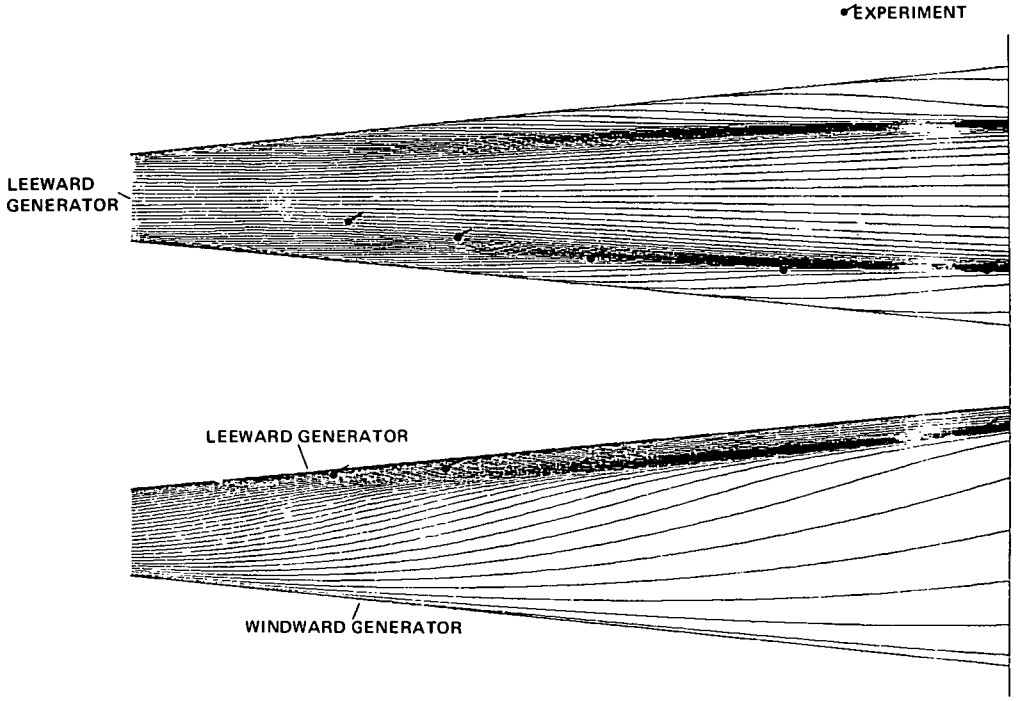

Fig. 3. Calculated limiting streamlines for flow past a sphere cone: θ_c = 5.6°; M_∞ = 14.2; Re = 6.2 × 10^5/ft; α = 18°. a) top view; b) side view.

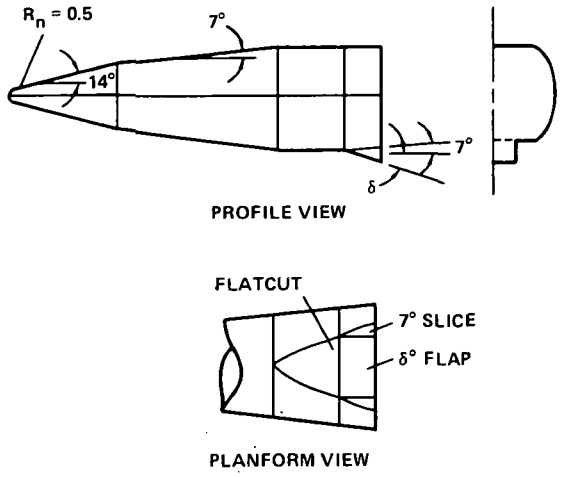

Fig. 4. Configurations which use flaps for control surfaces.

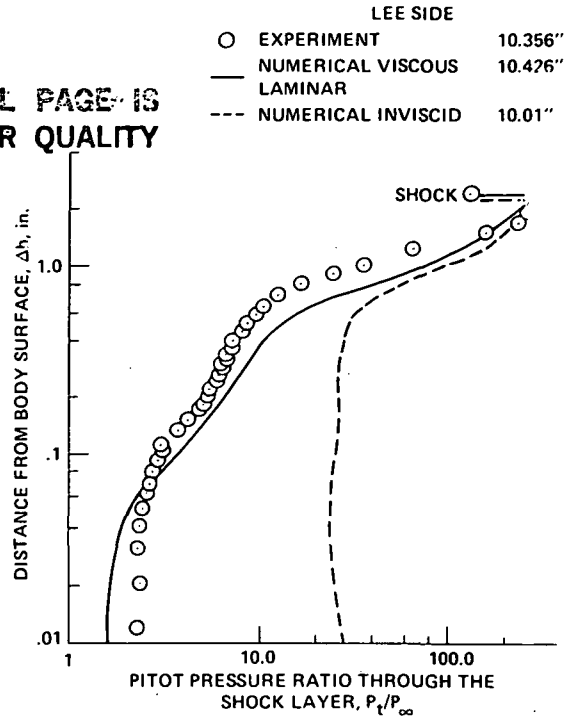

Fig. 6. Comparison between computations and experiment of the pitot-pressure variation through the shock layer: θ_c = 14°/7°; M_∞ = 10; $Re_D = 8.3 \times 10^4$; α = 10°; leeside X = 10.356.

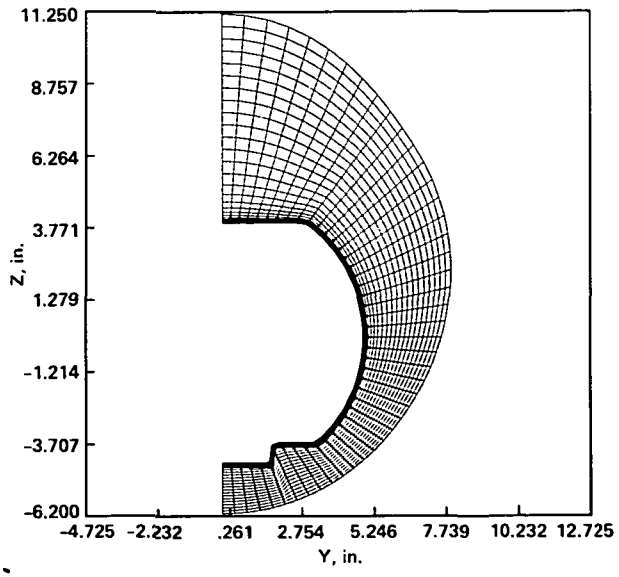

Fig. 5. Grid at X = 28.03 for a blunt 14°/7° sliced cone with a 9° deflected flap.

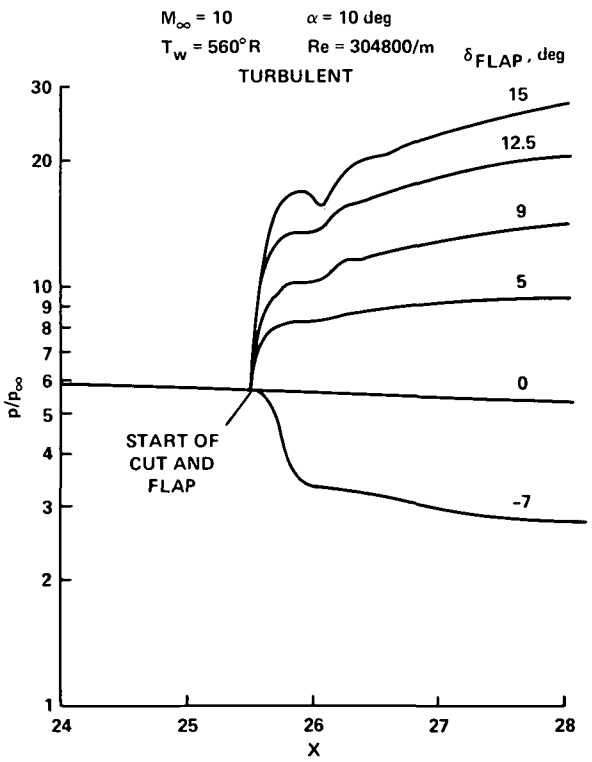

Fig. 7. Axial pressure distributions along the windward centerline for a blunt 14°/7° sliced cone for various flap deflections; M_∞ = 10; α = 10°; T_{wall} = 569°R; and turbulent Re = 304,800/m.

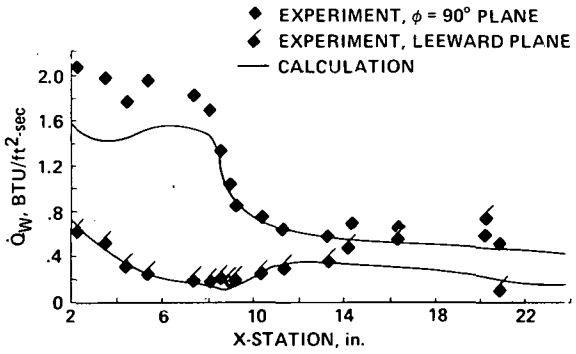

Fig. 8. Axial variation of the ϕ = 90° and the lee heat transfer: θ_c = 14°/7°: M_∞ = 10; $Re_D = 8.3 \times 10^4$; α = 10°.

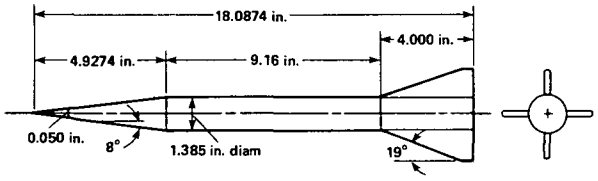

Fig. 9. Finned projectile geometry.

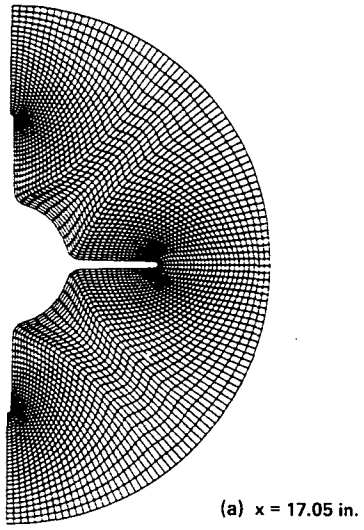

(a) x = 17.05 in.

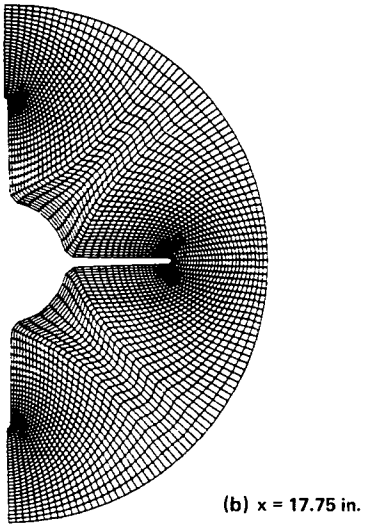

(b) x = 17.75 in.

Fig. 10. Typical computational meshes in the region of the fin.

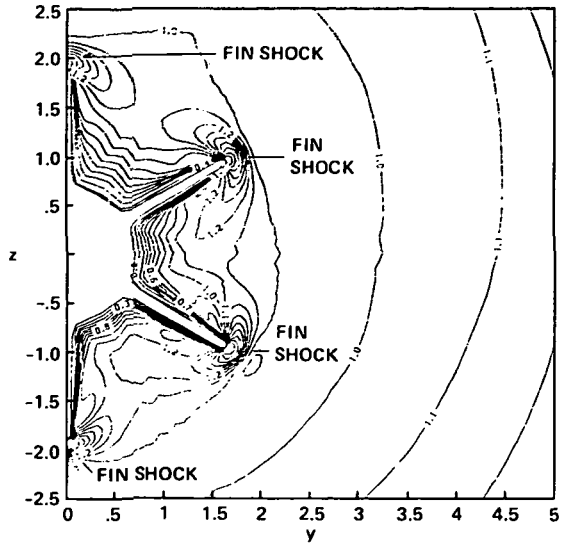

Fig. 11. Density contours for the projectile at X = 17.55 in. for $\alpha = 2°$, $M_\infty = 4$, and a turbulent $Re_L = 10^5$/in.

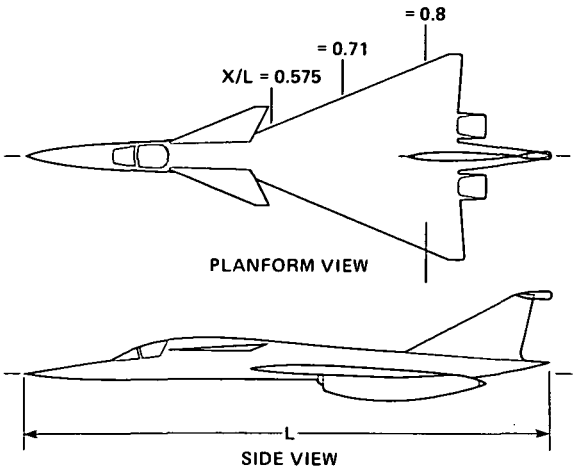

Fig. 14. Geometry of a generic supercruise fighter.

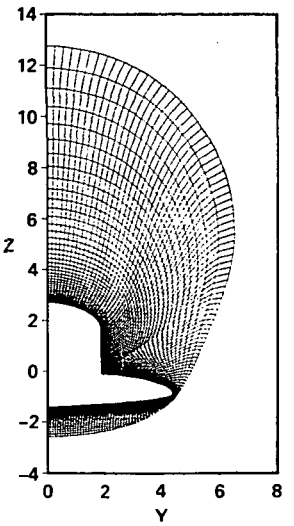

Fig. 12. Elliptic grid at X/L = 0.66.

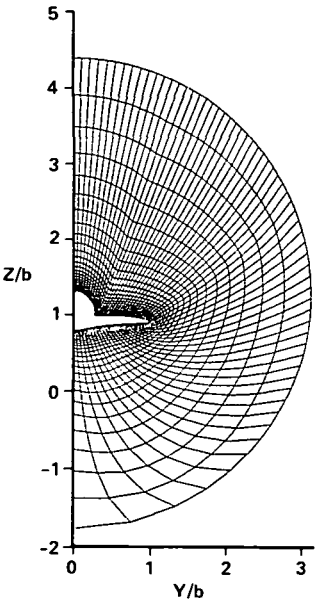

Fig. 15. Elliptic grid at X/L = 0.675 and $\alpha = 4°$.

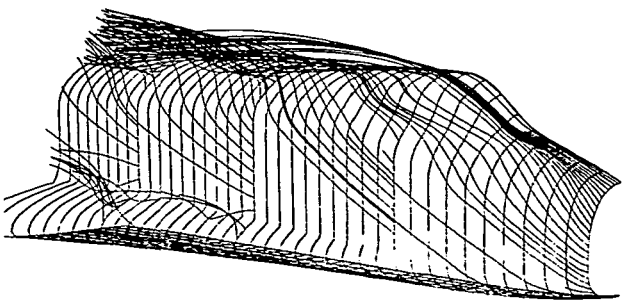

Fig. 13. Computational particle paths up to X/L = 0.66.

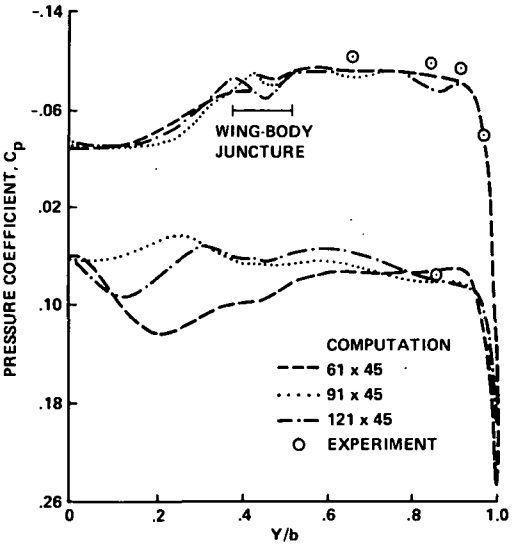

Fig. 16. Mesh effects at X/L = 0.575 and α = 4°.

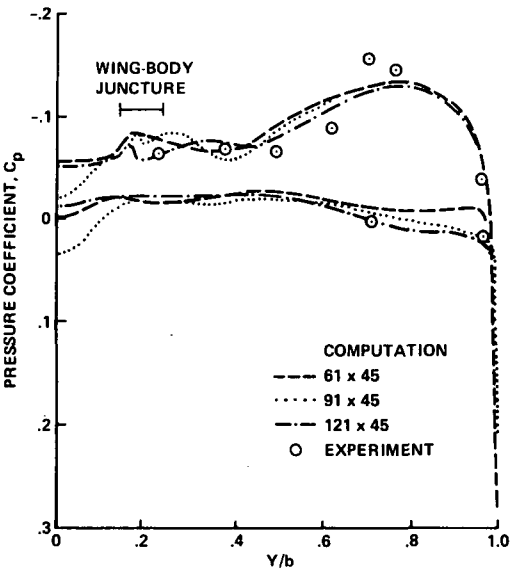

Fig. 17. Mesh effects at X/L = 0.8 and α = 4°.

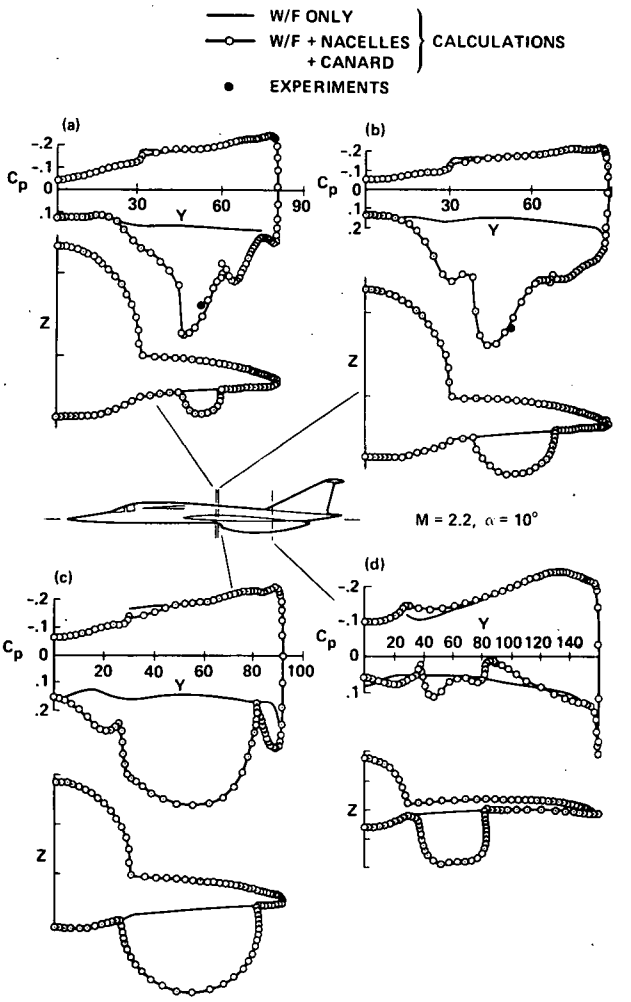

Fig. 18. Cp variations at different cross sections for wing-fuselage-nacelle at M_∞ = 2.2 and α = 10°.

1. Report No.	2. Government Accession No.	3. Recipient's Catalog No.
NASA TM-88237		

4. Title and Subtitle	5. Report Date
HIGH SPEED VISCOUS FLOW CALCULATIONS ABOUT COMPLEX CONFIGURATIONS	April 1986
	6. Performing Organization Code
7. Author(s)	8. Performing Organization Report No.
Denny S. Chaussee	A-86199
	10. Work Unit No.
9. Performing Organization Name and Address	
Ames Research Center Moffett Field, CA 94035	11. Contract or Grant No.
	13. Type of Report and Period Covered
12. Sponsoring Agency Name and Address	Technical Memorandum
National Aeronautics and Space Administration Washington, DC 20546	14. Sponsoring Agency Code 505-60

15. Supplementary Notes

Point of contact: Denny S. Chaussee, Ames Research Center, M/S 202-14, Moffett Field, CA 94035 (415) 694-6742 or FTS 464-6742

16. Abstract

Applications of the NASA Ames Parabolized Navier-Stokes (PNS) code to a variety of complex generic configurations is presented. The algorithm, boundary conditions, initial conditions, and grid generators are discussed as applied to these configurations.

The PNS code was used as the mainline procedure to numerically simulate the viscous supersonic flow over these generic configurations. The turbulence model that was used in this study is the Baldwin-Lomax model. The boundary conditions are the usual viscous no slip at the wall, and a characteristic procedure is used to fit the bow shock wave which is the outermost boundary. An elliptic grid generator is employed to discretize the flow domain. In addition, an equilibrium air capability has been incorporated into the code. It uses the curve fits of Tannehill, et al.

The flow regimes vary from a Mach No. of 2 up to 25. Both laminar and turbulent flow are considered. Varying angles of attack have also been computed. Configurations vary from simple cone-type bodies to lifting winged bodies, such as the space shuttle or the generic supersonic cruise fighter.

17. Key Words (Suggested by Author(s))	18. Distribution Statement
Computational fluid dynamics Hypersonics Complex configurations	Unlimited Subject Category - 34

19. Security Classif. (of this report)	20. Security Classif. (of this page)	21. No. of Pages	22. Price*
Unclassified	Unclassified	20	A02

*For sale by the National Technical Information Service, Springfield, Virginia 22161